Highly Uniform Large-Area (100 cm^2) Perovskite CH$_3$NH$_3$PbI$_3$ Thin-Films Prepared by Single-Source Thermal Evaporation

Guangxing Liang [†], Huabin Lan [†], Ping Fan *, Chunfeng Lan, Zhuanghao Zheng, Huanxin Peng and Jingting Luo

Shenzhen Key Laboratory of Advanced Thin Films and Applications, College of Physics and Energy, Shenzhen University, Shenzhen 518060, China; lgx@szu.edu.cn (G.L.); lanhb420@163.com (H.L.); lanchunfeng@gmail.com (C.L.); zhengzh@szu.edu.cn (Z.Z.); P2385284535@163.com (H.P.); luojt@szu.edu.cn (J.L.)

* Correspondence: fanping@szu.edu.cn; Tel.: +86-755-2653-6021

† These authors contributed equal to this work.

check for updates

Abstract: In this work, we report the reproducible preparation method of highly uniform large-area perovskite CH$_3$NH$_3$PbI$_3$ thin films by scalable single-source thermal evaporation with the area of 100 cm^2. The microstructural and optical properties of large-area CH$_3$NH$_3$PbI$_3$ thin films were investigated. The dense, uniform, smooth, high crystallinity of large-area perovskite thin film was obtained. The element ratio of Pb/I was close to the ideal stoichiometric ratio of CH$_3$NH$_3$PbI$_3$ thin film. These films show a favorable bandgap of 1.58 eV, long and balanced carrier-diffusion lengths. The CH$_3$NH$_3$PbI$_3$ thin film perovskite solar cell shows a stable efficiency of 7.73% with almost no hysteresis, indicating a single-source thermal evaporation that is suitable for a large area perovskite solar cell.

Keywords: single-source thermal evaporation; large-area perovskite; thin film; solar cell

1. Introduction

Hybrid organic-inorganic halide perovskites were considered to be an attractive superstar for low-cost solar cell applications due to their high-power conversion efficiency (PCE) and straightforward fabrication process [1,2]. In the past seven years, their rapid development led to PCE being raised from 3.8% to 22.7% by device optimization, perovskite composition and improved interface engineering [3,4]. The high performance is mainly due to the excellent properties of perovskite materials, such as extinction coefficients, electron and hole bipolar transport, medium band gap, small exciton binding energy and higher carrier diffusion length, etc. [5]. Although the highest certification efficiency of perovskite solar cells has exceeded 22% [6], the device areas are still small, with most of the areas being less than 1 cm^2. This raises issues such as peripheral effects, measurement contacts, film uniformity, etc. [7–10]. Therefore, the development of large-area perovskite solar cells is very important for future commercialization.

Nowadays, there are many preparation methods developed for high-efficiency perovskite solar cells, such as chemical solution process and vapor-assisted solution method [11,12]. However, chemical solution methods process with imperfect surface coverage and pinholes generated in large-area perovskite thin films fabrication, which seriously influences the solar cell's stability and efficiency [13–16]. Gu et al. [17] reported a facile seed printing method to produce a millimeter-scale perovskite single crystal film with controlled thickness and high yield through a printing process. This further proves that the perovskite single crystal film can be directly printed. Nirmal Peiris et al. [18] improved one-step deposition assisted by N$_2$ blow drying technique for depositing CH$_3$NH$_3$PbI$_3$ on

$TiO_2/ZrO_2/NiO$ screen printed electrodes, in which the low temperature treated carbon electrode method was then printed on the perovskite layer by a doctor blade. Through such methods, a significant PCE of 10.8% was achieved and the photocurrent and voltage were significantly improved. However, oxygen and moisture in the air can seriously affect the preparation of the perovskite thin film. The single source thermal evaporation method to prepare perovskite thin film under higher vacuum can eliminate the influence of oxygen and water vapor on the quality of the perovskite film. As far as we know, single-source thermal evaporation is a promising method for preparing the large-area perovskite thin films [19]. Single-source thermal evaporation is advantageous because it results in a highly uniform, pinhole-less, smooth thin films which are especially important for large-area solar cells to avoid the introduced short-circuits and benefit of the higher full fill factor and PCE [20]. In addition, single-source thermal evaporation requires no solvent and is, therefore, ideal for fabricating tandem solar cells and solar cells on flexible substrates [21].

In this work, we report the reproducible fabrication of highly uniform large-area perovskite $CH_3NH_3PbI_3$ thin films by scalable single-source thermal evaporation with the area of 100 cm^2. The microstructural and optical properties of large-area perovskite thin films were investigated.

2. Materials and Methods

2.1. $CH_3NH_3PbI_3$ Crystals and Powder Preparation

The 9.22 g PbI_2 (99.99%, Xi'an Polymer Light Technology, Xi'an, China) and 3.14 g CH_3NH_3I (99.5%, Xi'an Polymer Light Technology, Xi'an, China) were mixed in r-butyrolactone (30 mL, 99%, TCI Chemicals Pvt. Ltd., Shanghai, China) in a round bottom flask for 24 h with constant magnetic stirring (MYP11-2, Meiyingpu Instrument Meter Manufacturing Co., Ltd., Shanghai, China). Then, the $CH_3NH_3PbI_3$ perovskite precursor solution was transferred to a Petri dish and maintained at 160 °C on a hot plate until all $CH_3NH_3PbI_3$ perovskite precursor solutions were evaporated to give $CH_3NH_3PbI_3$ crystals. Finally, the $CH_3NH_3PbI_3$ crystals were grounded into powder as the film evaporation material.

2.2. $CH_3NH_3PbI_3$ Thin Films Preparation

A simplified schematic diagram of single-source thermal evaporation is shown in Figure 1. Prior to deposition, the large-area (10 cm × 10 cm) K9 (BK7) glass substrate was sequentially ultrasonically cleaned with acetone, ethanol and deionized water. Before evaporation, the substrate was treated with ozone for 20 min to improve the surface activity of the substrate 0.8 g of $MAPbI_3$ powder was placed into the evaporation boat (tungsten boat, Sky Technology Development, Shenyang, China), and when the pressure in the vacuum chamber was pumped down to below 1.5×10^{-3} Pa, the current work of the evaporation boat was rapidly increased to 140 A. Subsequently, the evaporation source temperature rapidly rose to the point where the $MAPbI_3$ powder evaporated. The substrate did not need to be heated, and the substrate rotated at 20 r/s to ensure a uniform film formation. The entire deposition process was about 3 min, and the actual deposited perovskite film thickness was about 500 nm. Lastly, the properties of $MAPbI_3$ thin films were improved by annealing at 140 °C for 20 min.
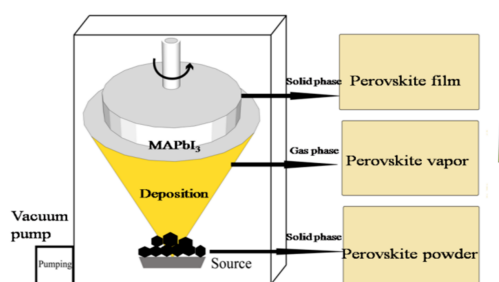

Figure 1. The simplified schematic diagram of the single-source thermal evaporation.

2.3. Device Fabrication

The perovskite solar cells with a device structure of ITO (coated-glass)/PEDOT:PSS (CLEVIOS PVP AI4083)/MAPbI$_3$ active layer/PC$_{61}$BM (99.5%, Xi'an Polymer Light Technology, Xi'an, China)/Ag was fabricated. A PEDOT:PSS (CLEVIOS PVP AI4083) aqueous solution was spin-coated onto a cleaned ITO glass substrate to form a 50 nm thick film (4500 rpm, 30 s), and the resulting PEDOT:PSS thin film was heated for 15 min at 150 °C and then transferred into a single source thermal evaporation system. The MAPbI$_3$ active layer was deposited on the PEDOT:PSS thin film by single-source thermal evaporation, and then annealed in a N$_2$-filled glovebox (Mikrouna GmbH, Shanghai, China) at 140 °C for 20 min. The PC$_{61}$BM solution (20 mg/mL in chlorobenzene, Xi'an Polymer Light Technology, Xi'an, China) was spin-coated on the complete perovskite MAPbI$_3$ thin film (3000 rpm, 30 s). Finally, the device fabrication was accomplished by evaporating a 100 nm thick silver film as the electrode.

2.4. Characterization

The large area MAPbI$_3$ thin film (100 cm^2) and the detected A, B, C, D and E regions are shown in Figure 2. The crystalline structures of the MAPbI$_3$ thin films were analyzed by X-ray diffraction technique (Ultima IV, Rigaku, Tokgo, Japan) operated at 40 kV and 40 mA with Cu Kα radiation (λ = 0.15406 nm). The surface morphology and composition of the MAPbI$_3$ thin films were analyzed by a SUPRA 55 scanning electron microscopy (SEM, SUPRA55, Zeiss, Oberkochen, Germany), and an energy dispersive X-ray microanalysis system (EDS, Bruker QUANTAX200, Bruker, Billerica, MA, USA). The thickness of MAPbI$_3$ thin films was measured by a DEKTAK XT profilometer (Bruker, Billerica, MA, USA). The Time-Resolved Photoluminescence was carried out at the Time-Resolved (FluoTime 300, PicoQuant GmbH, Shimadzu, Japan) at a peak of 780 nm. The optical transmittance properties of the MAPbI$_3$ thin films were obtained by spectrophotometer (Lambda 950, Perkin Elemer, Waltham, MA, USA) in the wavelength range of 300–1000 nm. The current density–voltage (*J–V*) curves of the MAPbI$_3$ thin film solar cells were recorded under simulated AM 1.5 G conditions (100 mW/cm^2) with a 2400 Source Measure Unit. The illuminated area of devices was precisely set with an area of 0.12 cm^2.
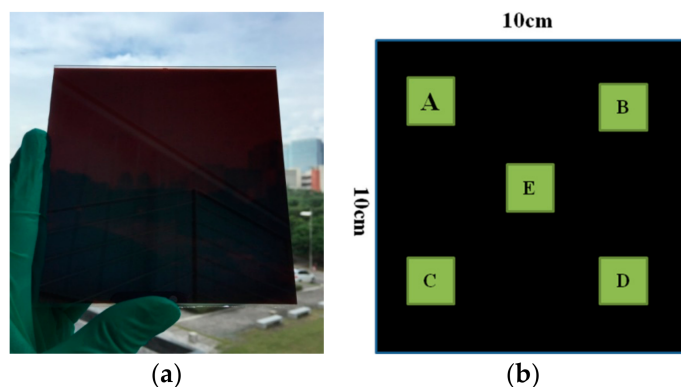

Figure 2. MAPbI$_3$ thin film (100 cm^2) (**a**), and the detected A, B, C, D and E regions in the large MAPbI$_3$ thin film (**b**).

3. Results and Discussion

Figure 3a shows the XRD patterns of A, B, C, D and E regions of the large-area perovskite MAPbI$_3$ thin film. It was found that the A, B, C, D and E regions of large-area perovskite MAPbI$_3$ thin films reveal strong characteristic diffraction peaks of (110), (220) and (330) planes of MAPbI$_3$, usually assigned to the tetragonal crystal structure of halide perovskite [22,23]. Also, the MAPbI$_3$ films in all regions did not have any impurity peak, in which the characteristic peak intensity was high, the crystallinity was high, and the preferred orientation of the film was obvious. Figure 3b–d show

the typical peak intensity change, FWHM (full width of half height) variation and grain size variation of the large-area perovskite (110), (220) and (310) respectively. Surprisingly, the peak intensities and half-widths of the (110), (220) and (310) characteristic peaks in regions A, B, C, D and E were almost the same. This shows that the large-area perovskite films have uniform crystallization in all regions with almost the same grain size. In addition, there was no PbI_2 or CH_3NH_3I detected in different regions, which indicates that it only goes through sublimation for the $MAPbI_3$ powder to thin film during the evaporation process.
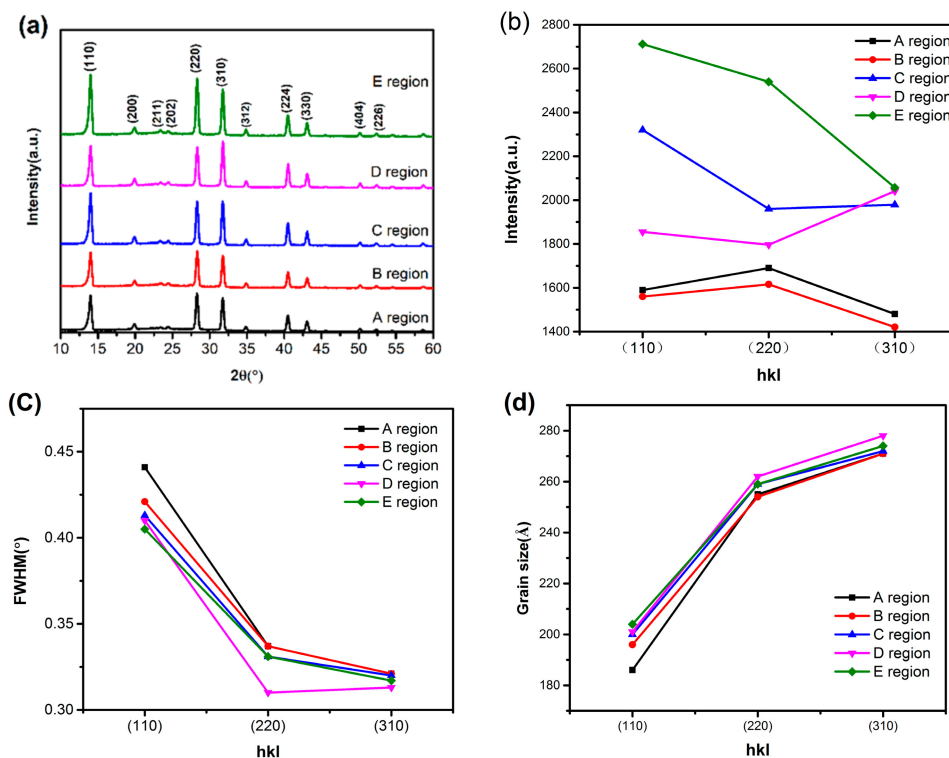

Figure 3. (**a**) XRD patterns of the large-area $MAPbI_3$ films prepared by single-source thermal evaporation, (**b**) the typical peak intensities change patterns, (**c**) the FWHM change patterns, and (**d**) the grain size change patterns.

The composition of the $MAPbI_3$ thin film is an important factor that affects the structure, electrical and optical properties of the absorber layer. The composition and elemental ratios of A, B, C, D and E regions of large-area $MAPbI_3$ films were analyzed by EDS. As shown in Figure 4, all five regions have two characteristic peaks at 2.48 and 3.98 keV, which corresponds to Pb and I elements. The energy-dispersive X-ray microanalysis system determines the ratio of Pb and I elements of large-area $MAPbI_3$ thin films as shown in Table 1. The Pb/I value for different regions were close to the theoretical stoichiometry of 0.333 indicating the prepared $MAPbI_3$ films with high compositional uniformity in a large area [24]. In addition, Figure 5 shows the distribution of Pb and I elements in different regions of large-area $MAPbI_3$ films. It shows that the locations of the Pb and I elements were nearly uniform across the entire plane, confirming the composition uniformity of large-area $MAPbI_3$ thin films.

The surface morphology of regions A, B, C, D and E of large-area $MAPbI_3$ thin films were measured by SEM. As shown in Figure 6, all regions of evaporated $MAPbI_3$ thin films exhibited full surface coverage with uniform grain size on the substrate. Even when the large-area was extremely dense and uniform. Figure 6f shows the cross-section of $MAPbI_3$ thin films. It can be found that the larger grains distributed evenly and the grains size approaches to the film thickness of about 500 nm. As shown in Table 2, the thickness of different region films was about 520 ± 10 nm. It can be concluded

that the significantly smoother and more uniform perovskite thin films prepared by the single-source evaporation is promising for large area high quality perovskite solar cells.
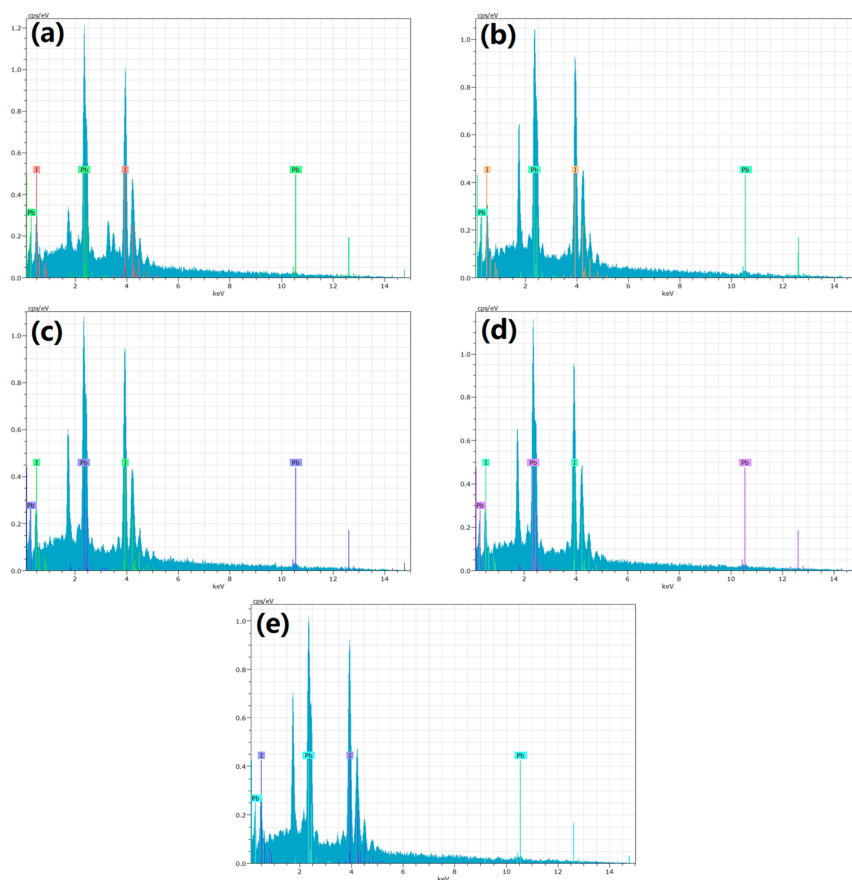

Figure 4. EDS spectral line pattern of A, B, C, D and E regions of MAPbI$_3$ thin films: (**a**) A region; (**b**) B region; (**c**) C region; (**d**) E region; (**e**) G region.

Table 1. The composition of as-deposited films and solvent annealed films determined by EDS analysis.

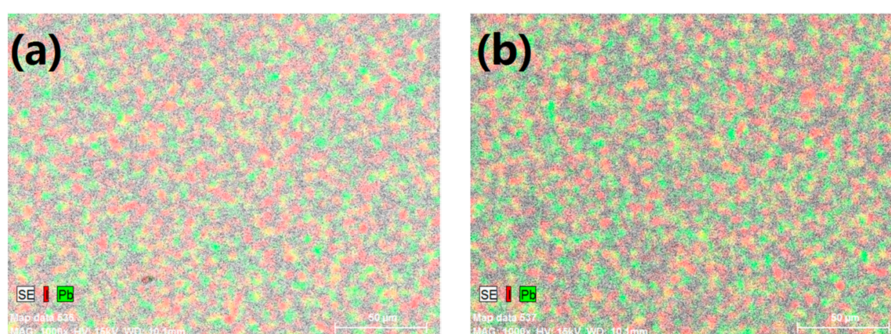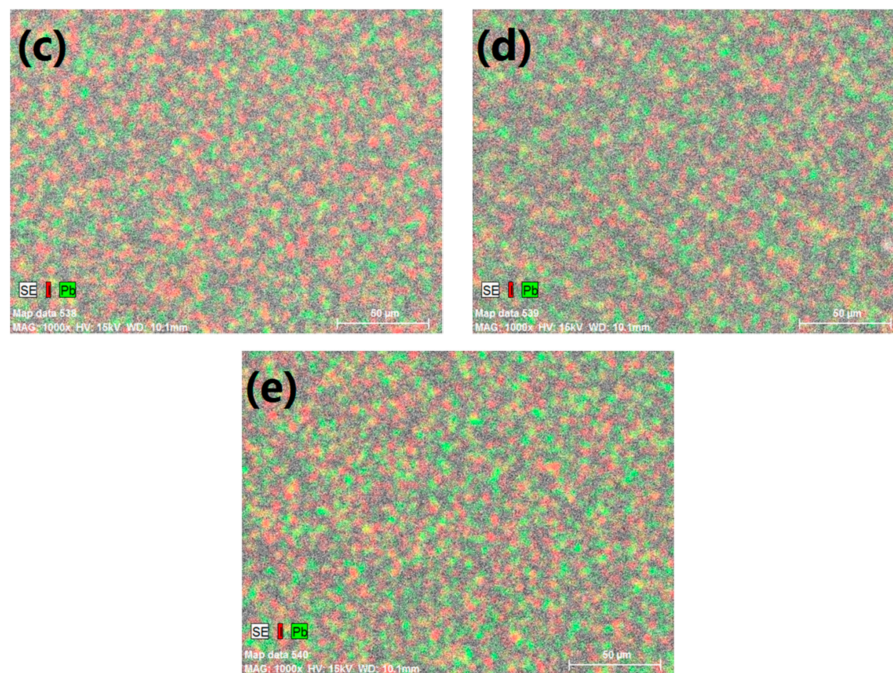| Sample	Pb (at.%)	I (at.%)	Pb/I
A region	27.93	72.07	0.38
B region	27.80	72.20	0.38
C region	27.69	72.31	0.38
D region	26.81	73.19	0.36
E region	25.84	74.16	0.35

Figure 5. *Cont.*

Figure 5. Distribution of Pb and I elements of A, B, C, D and E regions of large-area MAPbI$_3$ thin films: (**a**) A region; (**b**) B region; (**c**) C region; (**d**) D region; (**e**) E region.
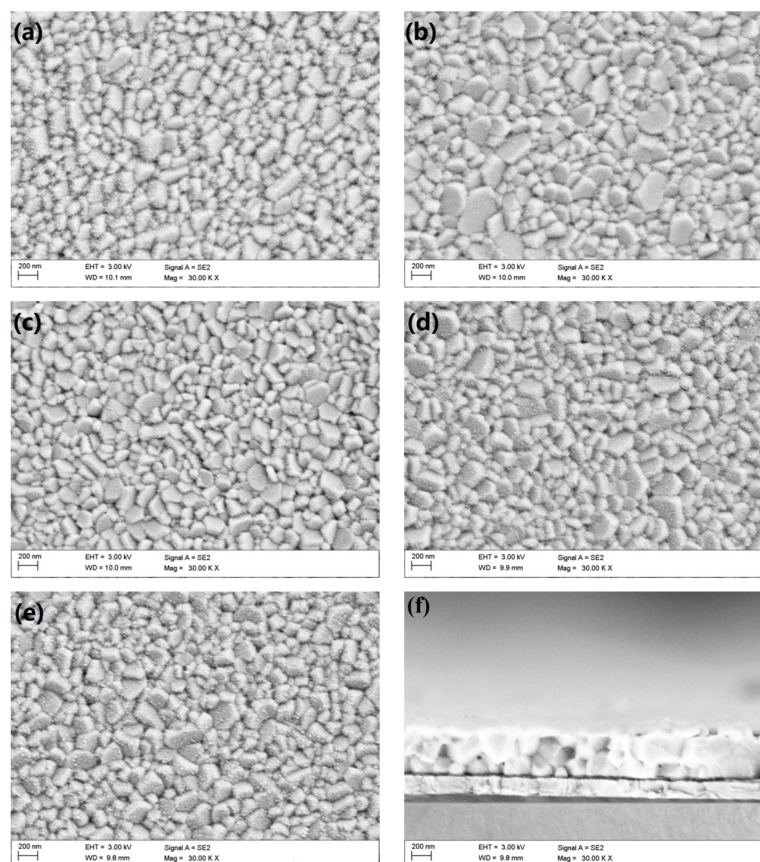

Figure 6. The surface morphology of A, B, C, D, and E regions: (**a**) A region; (**b**) B region; (**c**) C region; (**d**) D region; (**e**) E region; (**f**) Cross-section of MAPbI$_3$ thin film.

Table 2. The thickness of the MAPbI$_3$ layer in five areas on large-area thin film.

Region	Thickness
A	524.7 nm
B	512.5 nm
C	513.5 nm
D	510.1 nm
E	531.5 nm

To investigate the influence of perovskite film quality on carrier recombination character, time-resolved photoluminescence (TRPL) was carried out by measuring the PL decay of the emission peaks at 760 nm with an excitation wavelength of 532 nm, indicating the defect states and recombination process of perovskite films, as shown in Figure 7. It shows that the time-resolved PL spectra of the A, B, C, D and E regions of large-area perovskite glass/MAPbI$_3$ thin film demonstrated ultrafast lifetimes (average lifetime of about 9 ns, respectively I_A = 10.6 ns, I_B = 7.4 ns, I_C = 8.2 ns, I_D = 10.4 ns, I_E = 8.4 ns) and much slower decay processes after being fitted by the double-exponential decay function $I = (A_1\tau_1{}^2 + A_2\tau_2{}^2)/(A_1\tau_1 + A_2\tau_2)$ where τ_1 is the faster component of trap-mediated nonradiative recombination and τ_2 is the slower component correlated to radiative recombination [25–27]. According to the perovskite life length and the diffusion coefficient of electrons and holes D, and according to the formula $L_D{}^2 = Dt_e$, the electron and the hole average diffusion lengths of 184 nm and 156 nm were deduced respectively, which is higher than CH$_3$NH$_3$PbI$_3$ having prepared by solution method (about 100 nm) [28]. The formation of large grains can reduce the recombination of photoelectron-hole pairs and reduce the defect state of large-area perovskite MAPbI$_3$ thin films, which can increase the diffusion distance of carriers [29]. These high-quality films are promising for use in large-area perovskite solar cells.
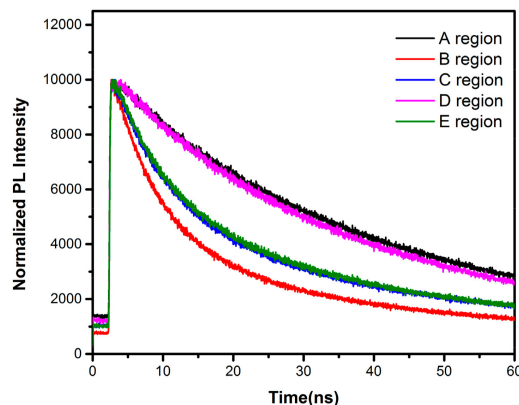

Figure 7. TRPL lifetime in regions A, B, C, D and E of large-area perovskite MAPbI$_3$ thin films.

Figure 8 shows the transmission spectra of A, B, C, D and E regions of large-area perovskite MAPbI$_3$ thin films. The transmissivity curves of all regions almost coincide, indicating good uniformity of the large-area perovskite thin films. There was a sharp absorption edge at 780 nm indicating that the large-area perovskite MAPbI$_3$ thin films with good crystallinity leads to the wide range of light absorption over the entire visible region. The bandgap energy in the A, B, C, D and E regions of the large-area perovskiteMAPbI$_3$ thin film was calculated from:

$$Ah_\gamma = A(h_\gamma - E_g)^n \tag{1}$$

where α is the absorption coefficient, h_γ is the photon energy, n depends on the nature of transition, A is the constant, and E is the bandgap energy [30]. As shown in Figure 9, The calculated band gap

of each region of large-area perovskite $MAPbI_3$ thin film is about 1.58 eV, which was close to the theoretical value of 1.55 eV reported by Baikie's group [31].
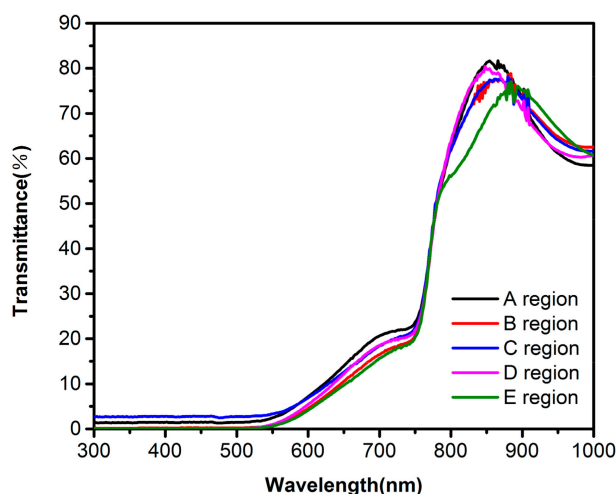

Figure 8. The transmission spectra of A, B, C, D and E regions of large-area perovskite $MAPbI_3$ thin films.
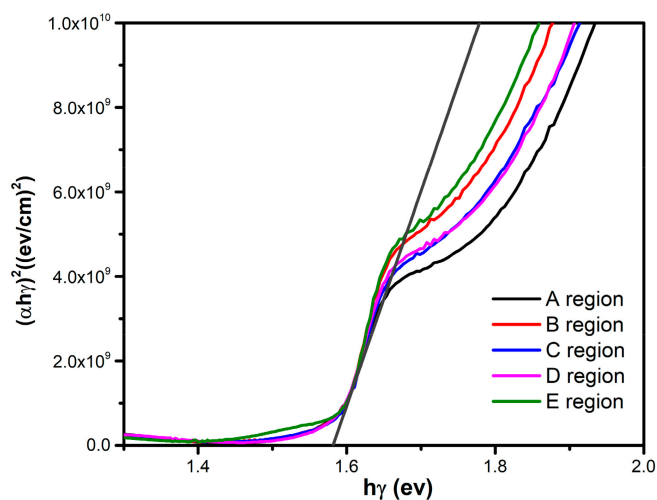

Figure 9. Optical band gap estimation of A, B, C, D and E regions of large-area perovskite $MAPbI_3$ thin films.

Figure 10a shows the device structure of $MAPbI_3$ thin film solar cells with ITO coated-glass/ PEDOT:PSS/$MAPbI_3$/$PC_{61}BM$/Ag and the cross-section of the solar cell device was shown in Figure 10b. It can be found that the $MAPbI_3$ thin film solar cell distinguishes individual PEDOT:PSS and $MAPbI_3$ layers clearly but obscures PCBM and Ag. The device performance was assessed using current density–voltage (*J*–*V*) sweeps under simulated sunlight. As shown in Figure 10c, the PCE of the champion cell was 7.73% with an open circuit voltage (V_{OC}) of 0.89 V and a short circuit current (J_{SC}) of 12.80 mA/cm^2. In particular, there was almost no photocurrent hysteresis in the *J*–*V* curve of $MAPbI_3$ perovskite solar cells. This result shows that the single-source thermal evaporation $MAPbI_3$ yields efficient solar cells with a relatively simple and planar cell architecture. The statistics of the PCE based on 20 devices are shown in Figure 10d and an average of 6.78% was obtained.
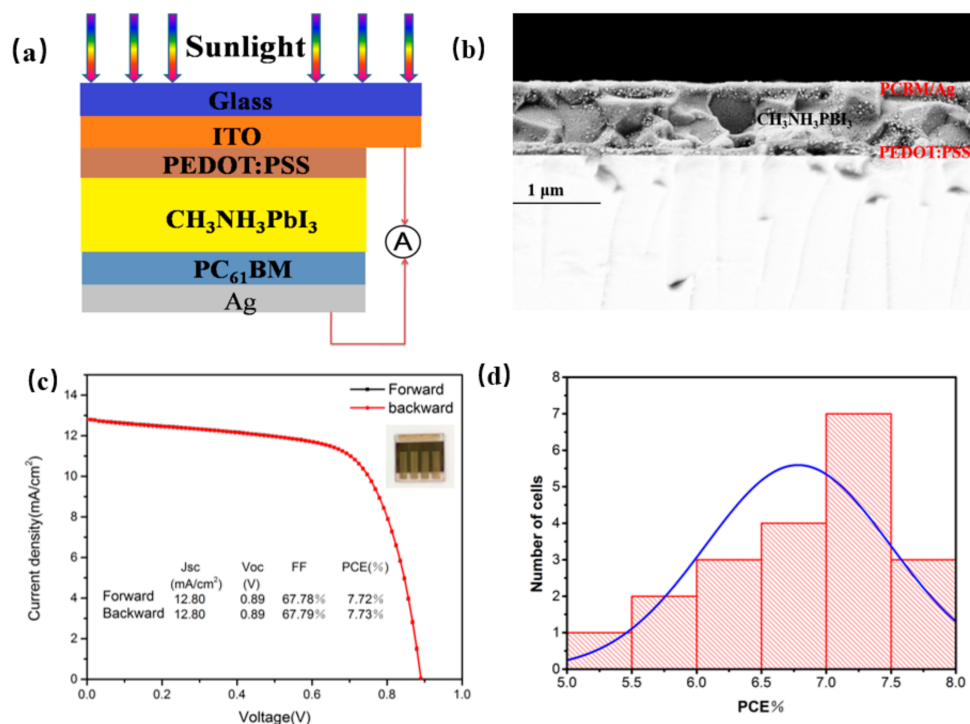
Figure 10. (**a**) Architecture of the devices, (**b**) cross-section of solar cell, (**c**) current density–voltage (*J*–*V*) curve of the champion single-source thermal evaporation MAPbI$_3$ device, and (**d**) histograms of power conversion efficiency (PCE) of 20 cells.

4. Conclusions

In summary, we report a facile, efficient and reproducible new method for the fabrication of large-area (10 cm × 10 cm) perovskiteMAPbI$_3$ thin film by single-source thermal evaporation. The dense, uniform, less porous and high crystallinity of large-area perovskite thin films can be obtained. The element ratio of Pb/I was close to the ideal stoichiometric ratio of CH$_3$NH$_3$PbI$_3$ thin film. In addition, there is no PbI$_2$ or CH$_3$NH$_3$I detected in different regions, which indicates that it only goes through sublimation for the MAPbI$_3$ powder to thin film during the evaporation process. These films exhibit a favorable bandgap of 1.58 eV, long and balanced carrier-diffusion lengths. The CH$_3$NH$_3$PbI$_3$ thin film perovskite solar cell shows a stable efficiency of 7.73% with almost no hysteresis, indicating that the single-source thermal evaporation is suitable for the large area and efficient perovskite solar cell.

Author Contributions: Conceptualization, P.F. and G.L.; Formal Analysis, G.L. and H.L.; Investigation, G.L., H.L., C.L. and H.P.; Resources, P.F. and G.L.; Writing-Original Draft Preparation, G.L. and H.L.; Writing-Review & Editing, G.L., P.F., Z.Z. and J.L.; Funding Acquisition, P.F. and G.L.

Conflicts of Interest: The authors declare no conflict of interest.

References

1.　Nie, W.; Tsai, H.; Asadpour, R.; Blancon, J.C.; Neukirch, A.J.; Gupta, G.; Crochet, J.J.; Chhowalla, M.; Tretiak, S.; Alam, M.A.; et al. Perovskite solar cells with millimeter-scale grains. *Science* **2015**, *347*, 522–525. [CrossRef] [PubMed]

2.　Gao, P.; Gratzel, M.; Nazeeruddin, M.K. Organohalide lead perovskites for photovoltaic applications. *Energy Environ. Sci.* **2014**, *7*, 2448–2463. [CrossRef]

3.　Habibi, M.; Rahimzadeh, A.; Bennouna, I.; Eslamian, M. Defect-free large-area (25 cm^2) light absorbing perovskite thin films made by spray coating. *Coatings* **2017**, *7*, 42. [CrossRef]

4.　Yan, J.; Ke, X.; Chen, Y.; Zhang, A.; Zhang, B. Effect of modulating the molar ratio of organic to inorganic content on morphology, optical absorption and photoluminescence of perovskite CH$_3$NH$_3$PbBr$_3$ films. *Appl. Surf. Sci.* **2015**, *351*, 1191–1196. [CrossRef]

5.　Burschka, J.; Pellet, N.; Moon, S.J.; Humphry-Baker, R.; Gao, P.; Nazeeruddin, M.K.; Graetzel, M. Sequential deposition as a route to high-performance perovskite-sensitized solar cells. *Nature* **2013**, *499*, 316–319. [CrossRef] [PubMed]

6.　Green, M.A.; Ho-Baillie, A.; Snaith, H.J. The emergence of perovskite solar cells. *Nat. Photonics* **2014**, *8*, 506–514. [CrossRef]

7.　Chen, W.; Wu, Y.; Yue, Y.; Liu, J.; Zhang, W.; Yang, X.; Chen, H.; Bi, E.; Ashraful, I.; Gratzel, M.; et al. Efficient and stable large-area perovskite solar cells with inorganic charge extraction layers. *Science* **2015**, *350*, 944–948. [CrossRef] [PubMed]

8.　Zhang, X.; Ren, X.; Liu, B.; Munir, R.H.; Zhu, X.; Yang, D.; Li, J.; Liu, Y.; Smilgies, D.M.; Li, R.; et al. Stable high efficiency two-dimensional perovskite solar cells via cesium doping. *Energy Environ. Sci.* **2017**, *10*, 2095–2102. [CrossRef]

9.　Chen, H.; Zheng, X.; Li, Q.; Yang, Y.; Xiao, S.; Hua, C.; Bai, Y.; Zhang, T.; Wong, K.; Yang, S. Amorphous precursor route to the conformable oriented crystallization of CH$_3$NH$_3$PbBr$_3$ in mesoporous scaffolds: Toward efficient and thermally stable carbon-based perovskite Solar Cells. *J. Mater. Chem. A* **2016**, *4*, 12897–12912. [CrossRef]

10.　Wang, Q.; Dong, Q.; Li, T.; Gruverman, A.; Huang, J. Thin insulating tunneling contacts for efficient and water-resistant perovskite solar cells. *Adv. Mater.* **2016**, *28*, 6734–6739. [CrossRef] [PubMed]

11.　Richardson, G.; Kane, J.O.; Niemann, R.G.; Peltola, T.A.; Foster, J.M.; Cameron, P.J.; Walker, A.B. Can slow-moving ions explain hysteresis in the current–voltage curves of perovskite solar cells? *Energy Environ. Sci.* **2016**, *9*, 1476–1485. [CrossRef]

12.　Cao, D.; Stoumpos, C.C.; Farha, O.K.; Hupp, J.T.; Kanatzidis, M.G. 2D homologous perovskites as light-absorbing materials for solar cell applications. *J. Am. Chem. Soc.* **2015**, *137*, 7843–7850. [CrossRef] [PubMed]

13.　Rong, Y.; Hou, X.; Hu, Y.; Mei, A.; Liu, L.; Wang, P.; Han, H. Synergy of ammonium chloride and moisture on perovskite crystallization for efficient printable mesoscopic solar cells. *Nat. Commun.* **2017**, *8*, 14555.

14.　Nenon, D.P.; Christians, J.A.; Wheeler, L.M.; Blackburn, J.L.; Sanehira, E.M.; Dou, B.; Olsen, M.L.; Zhu, K.; Berry, J.J.; Luther, J.M. Structural and chemical evolution of methylammonium lead halide perovskites during thermal processing from solution. *Energy Environ. Sci.* **2016**, *9*, 2072–2082. [CrossRef]

15.　Heo, J.H.; Han, H.J.; Kim, D.; Ahn, T.K.; Im, S.H. Hysteresis-less inverted CH$_3$NH$_3$PbI$_3$ planar perovskite hybrid solar cells with 18.1% power conversion efficiency. *Energy Environ. Sci.* **2015**, *8*, 1602–1608. [CrossRef]

16.　Rehman, W.; McMeekin, D.P.; Patel, J.B.; Milot, R.L.; Johnston, M.B.; Snaith, H.J.; Herz, L.M. Photovoltaic mixed-cation lead mixed-halide perovskites: Links between crystallinity, photo-stability and electronic properties. *Energy Environ. Sci.* **2017**, *10*, 361–369. [CrossRef]

17.　Gu, Z.; Huang, Z.; Li, C.; Li, M.; Song, Y. A general printing approach for scalable growth of perovskite single-crystal films. *Sci. Adv.* **2018**, *4*, eaat2390. [CrossRef] [PubMed]

18.　Nirmal Peiris, T.A.; Baranwal, A.K.; Kanda, H.; Fukumoto, S.; Kanaya, S.; Cojocaru, L.; Bessho, T.; Miyasaka, T.; Segawa, H.; Ito, S. Enhancement of the hole conducting effect of NiO by a N$_2$ blow drying method in printable perovskite solar cells with low-temperature carbon as the counter electrode. *Nanoscale* **2017**, *9*, 5475–5482. [CrossRef] [PubMed]

19.　Liang, G.; Fan, P.; Luo, J.; Gu, D.; Zheng, Z. A promising unisource thermal evaporation for in situ fabrication of organolead halide perovskite CH$_3$NH$_3$PbI$_3$ thin film. *Prog. Photovolt. Res. Appl.* **2015**, *23*, 1901–1907. [CrossRef]

20.　Fan, P.; Gu, D.; Liang, G.; Luo, J.; Chen, J.; Zheng, Z.; Zhang, D. High-performance perovskite CH$_3$NH$_3$PbI$_3$ thin films for solar cells prepared by single-source physical vapour deposition. *Sci. Rep.* **2016**, *6*, 29910. [CrossRef] [PubMed]

21.　Borchert, J.; Milot, R.L.; Patel, J.B.; Davies, C.L.; Wright, A.D.; Maestro, L.M.; Snaith, H.J.; Herz, L.M.; Johnston, M.B. Large-area, highly uniform evaporated for mamidinium lead triiodide thin films for solar cells. *ACS Energy Lett.* **2017**, *2*, 2799–2804. [CrossRef]

22. Chen, Q.; Zhou, H.; Hong, Z.; Luo, S.; Duan, H.; Wang, H.; Liu, Y.; Li, G.; Yang, Y. Planar Heterojunction perovskite solar cells via vapor-assisted solution process. *J. Am. Chem. Soc.* **2014**, *136*, 622–625. [CrossRef] [PubMed]

23. Kim, H.B.; Choi, H.; Jeong, J.; Kim, S.; Walker, B.; Song, S.; Kim, J.Y. Mixed solvents for the optimization of morphology in solution-processed, inverted-type perovskite/fullerene hybrid solar cells. *Nanoscale* **2014**, *6*, 6679–6683. [CrossRef] [PubMed]

24. Zhao, Y.; Zhu, K. CH$_3$NH$_3$Cl-assisted one-step solution growth of CH$_3$NH$_3$PbI$_3$: Structure, charge-carrier dynamics, and photovoltaic properties of perovskite solar cells. *J. Phys. Chem. C* **2014**, *118*, 9412–9418. [CrossRef]

25. Chen, W.; Zhang, J.; Xu, G.; Xue, R.; Li, Y.; Zhou, Y.; Hou, J.; Li, Y. A semitransparent inorganic perovskite film for overcoming ultraviolet light instability of organic solar cells and achieving 14.03% efficiency. *Adv. Mater.* **2018**, *30*, 1800855. [CrossRef] [PubMed]

26. Wang, J.; Cao, R.; Da, P.; Wang, Y.; Hu, T.; Wu, L.; Lu, J.; Hen, X.; Xu, F.; Zheng, G.; et al. Purcell effect in an organic-inorganic halide perovskite semiconductor microcavity system. *Appl. Phys. Lett.* **2016**, *108*, 022103. [CrossRef]

27. Duan, J.; Zhao, Y.; He, B.; Tang, Q. Simplified perovskite solar cell with 4.1% efficiency employing inorganic CsPbBr$_3$ as light absorber. *Small* **2018**, *14*, 1704443. [CrossRef] [PubMed]

28. Kim, J.; Kim, G.; Kim, T.; Kwon, S.; Back, H.; Lee, J.; Lee, S.; Kang, H.; Lee, K. Efficient planar-heterojunction perovskite solar cells achieved via interfacial modification of a sol-gel ZnO electron collection layer. *J. Mater. Chem. A* **2014**, *2*, 17291–17296. [CrossRef]

29. Lan, C.; Zhao, S.; Zhang, C.; Liu, W.; Hayase, S.; Ma, T. Concentration gradient-controlled growth of large-grain CH$_3$NH$_3$PbI$_3$ films and enhanced photovoltaic performance of solar cells under ambient conditions. *CrystEngComm* **2016**, *18*, 9243–9251. [CrossRef]

30. Muller, J.; Nowoczin, J.; Schmitt, H. Composition, structure and optical properties of sputtered thin films of CuInSe$_2$. *Thin Solid Films* **2006**, *496*, 364–370. [CrossRef]

31. Baikie, T.; Fang, Y.; Kadro, J.M.; Schreyer, M.; Wei, F.; Mhaisalkar, S.G.; Graetzeld, M.; Whitec, T.J. Synthesis and crystal chemistry of the hybrid perovskite (CH$_3$NH$_3$) PbI$_3$ for solid-state sensitised solar cell applications. *J. Mater. Chem. A* **2013**, *1*, 5628–5641. [CrossRef]